

Evaluation of neutron beam characteristics for D-BNCT01 facility

Jun-Yang Chen^{1,2,3,4}, Jian-Fei Tong^{1,3,4}, Zhi-Liang Hu^{1,3,4}, Xue-Fen Han^{1,2,3}, Bin Tang^{1,3}, Qian Yu^{1,2,3},
Rui-Qiang Zhang^{1,3}, Chong-Guang Zhao^{1,3}, Jun Xu^{1,3}, Shi-Nian Fu^{1,2,3},
Bin Zhou^{1,3,4,*}, Tian-Jiao Liang^{1,2,3,4,*}

¹Institute of High Energy Physics, Chinese Academy of Sciences (CAS), Beijing, 100049, China

²University of Chinese Academy of Sciences (UCAS), Beijing, 100049, China

³Spallation Neutron Source Science Center, Dongguan, 523803, China

⁴Guangdong-Hong Kong-Macao Joint Laboratory for Neutron Scattering Science and Technology, Dongguan 523803, China

*Corresponding author, binzhou@ihep.ac.cn (Bin Zhou); tjliang@ihep.ac.cn (Tianjiao Liang)

Abstract

An accelerator-based Boron Neutron Capture Therapy (AB-BNCT) experimental facility called D-BNCT01 has been recently completed and is currently able to generate a high-intensity neutron beam for BNCT related research. In this study, we perform several experiments involving water phantoms to validate the Monte Carlo simulation results and analyze the neutron beam characteristics. According to our measurements, D-BNCT01 may generate a neutron flux about 1.2×10^8 n/cm²/s at the beam port using a 5 kW proton beam. Our results, also show that the thermal neutron flux depth distribution inside the water phantom is in good agreement with simulations. We conclude that D-BNCT01 may be effectively employed for BNCT research.

Keywords: Neutron beam; Boron Neutron Capture Therapy; Water phantom

1. Introduction

Boron Neutron Capture Therapy (BNCT) is an advanced therapeutic modality where the boron agent is administrated to the patient, and the boron accumulates in the tumor cells [1-3]. The patient is then irradiated with neutrons having a suitable energy spectrum and intensity. Since reactor-based neutron sources have several drawbacks, accelerator-based Boron Neutron Capture Therapy (AB-BNCT) received much attention, especially because such facilities can be installed in hospitals. In particular, many research groups have been focusing on the development of compact accelerator-based neutron sources [4-6].

In our cases, we have built an experimental, accelerator-based, BNCT instrument within the Spallation Neutron Source Science Center, which is called D-BNCT01. Besides, we are developing the BNCT facility D-BNCT02, which will be installed in a hospital in the future. The proton energy of D-BNCT02 is 2.8 MeV and the beam power is 50 kW. The lithium target is used in this case. As for the D-BNCT01, the neutron beam has been successfully generated using a low-current 3.5 MeV proton beam in 2019. Since then, the proton current has been gradually increased and the whole facility has been eventually completed in 2020. Currently, we are performing cell and animal trials with the D-BNCT01 facility.

Beam Shaping Assembly (BSA) is usually designed to exploit Monte Carlo simulations. Before conducting the trials on animals, however, the validity of the simulation-based design should be confirmed, and the characteristic of the neutron field should be analyzed. To this aim, several neutron monitoring and spectrum measurement techniques have been developed [7-8]. However, as this device generates an epi-thermal neutron beam, it is difficult to measure the neutron intensity and spectrum directly. Since our main purpose is to assess the quality of the neutron field rather than developing innovative beam probing techniques, we perform measurements of the thermal neutron flux distribution using a water phantom. Moreover, the neutronic measurement related to proton energy 3.5 MeV for BNCT facility has not been reported.

In this work, we employ three methods to measure the thermal neutron flux in the water phantom, including gold wire activation [9], Cu foil activation [10], and lithium-based scintillator using a scanning system [11]. In the following, we first introduce the simulation method and the measurement schemes, and then we present the results of a systematic comparison between the experimental and simulation results. Finally, we analyze the validity of the designed facility.

2. Methodology

2.1 Monte Carlo simulation

The phantom experiments are simulated using Monte Carlo methods. In particular, we employ the code MCNPX2.5 [12]. This code is a general-purpose Monte Carlo radiation transport code that tracks nearly all particles at nearly all energies. Accordingly, the general source definition of this code is the SDEF card. And the angle-dependent energy spectrum of the neutron source term can be defined by using this card (e.g., $\text{erg}=\text{fdir}=\dots$). For simulating neutron transportation accurately and saving computing time, the particle source term in the SDEF card should be considered carefully. As the neutron yield of the 3.5 MeV proton beam is 4.0×10^{-4} neutron/proton, the statistical precision of the neutron tally is hard to meet the requirement with the simulation beginning with the proton beam and setting the neutron tally in the water phantom. It is noted that the estimated relative error R is proportional to $1/N^{1/2}$, where N is the number of histories. And the consumed computing time T is proportional to N , which means if $R=0.1$ when $T=1$ hour, the 100 hours will be required to obtain the $R=0.01$. The way of increasing the total number of histories to be run in the problem is useless. However, because producing one neutron needs nearly 40 thousand protons [13], setting the second neutron source term is an effective way to increase the precision and save computing time when we tally the neutron flux in the terminal of the instrument. Thus, the simulation is divided into two steps.

The first step is proton beam simulation. In this step, only a cylinder made of lithium is included in the model, and its diameter and thickness are 10 cm and 300 μm , respectively. This size of the lithium layer is nearly consistent with the actual lithium target structure. The proton beam is perpendicular to the lithium surface, and the divergence of this beam is not considered in this case. It is noted that the cross-section library used for the proton reacting with lithium is from endf70prot of ENDF/VII [14-15]. However, the accuracy of these cross-sections for the proton energy 3.5 MeV should be validated by further experiment. As for neutron tally in this step, the F1 tally card of the MCNPX2.5 code is used. It is noted that the energy spectra of the emitting neutron from the lithium layer are quite different at different emitting angles. Generally, the average energy of the neutron emitting from the proton beam direction is relatively higher. Thus, when obtaining the neutronic information of the neutron emitting from the lithium layer, the neutron spectra of different angles are tallied by using the c card and e card simultaneously.

The second step is to set the neutron source term in the MCNPX2.5 for obtaining the neutron flux in the water phantom. Similarly, according to the tallied result of the first step, the related neutron source term can be defined. It is noted that the angle-dependent neutron spectra are considered in this second neutron source term. Importantly, in this step, the geometry used for the simulation is close to real structure of the facility, which is shown in Fig.1. Obviously, using the reasonable neutron source instead of the proton source as the start particle for the actual model simulation can obtain the high precision result with less computing time.

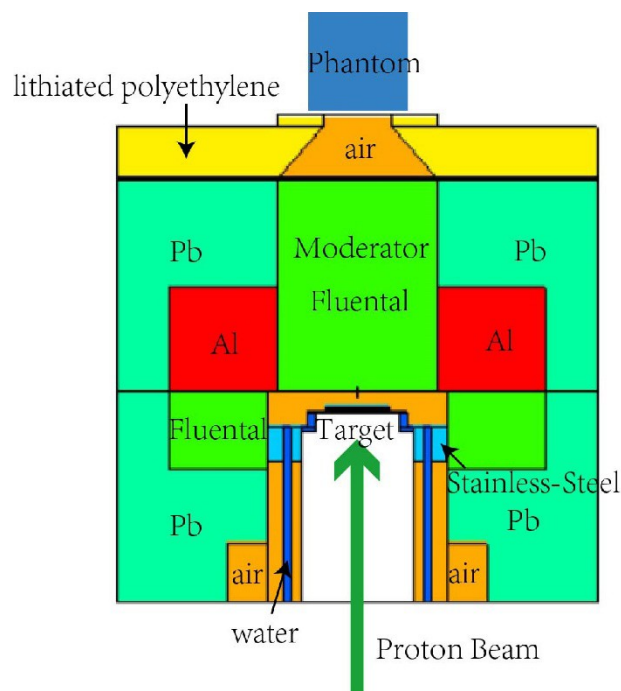


Fig.1 (Color online) Simulation model. The orange area represents air, red area is Al, green area is Flualtal, yellow area is lithiated polyethylene, blue area is water, sky blue area is Pb, and the light blue area denotes the stainless-steel vessel.

The BSA material and configuration are truthfully modeled in the simulation. The moderator materials are Flualtal and Al. And the reflector material is Pb. The collimator material is lithiated polyethylene. As the target system will influence the terminal neutron result, and its structure is relatively complex, we should establish a reasonable geometric model without losing simplicity. In the simulation of the second step, the target system is made of three layers: the lithium layer, the copper layer, and the mixed copper-water layer. The refrigeration contains water, which is an important material for neutron transportation as hydrogen can effectively moderate the neutron. This structure should be considered in the model. However, as the configuration of the refrigeration is complicated, and some tiny components have little influence on neutron transportation, we use the mixed copper-water layer to model this structure. The atomic compositions of copper and water are nearly the same as the realistic structure. And for the same reason, the inlet and outlet pipes are also included in the model. Besides, notice that the shielding configuration is not included in our simulations because the shielding has less influence on the water phantom. In fact, it just absorbs the unnecessary neutron. Including the shielding structure into the model means effective variance reduction techniques should be applied, which is unimportance for our purpose.

2.2 Water phantom

The following irradiation measurements employ a water phantom with walls made of polymethyl methacrylate (PMMA) and size is 200 mm × 200 mm × 200 mm. The thickness of the phantom wall at the front side is 2 mm, and that on the other side is 5 mm. The phantom is filled with deionized water. During the experiment, the phantom is close to the beam port, and the center of the phantom is placed consistently. The experimental setup is shown in Fig. 2.

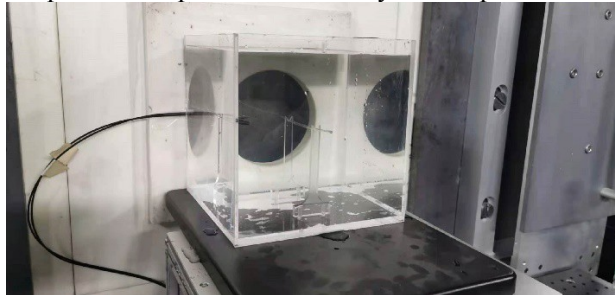


Fig.2 (Color online) The water phantom used in our measurements.

2.3 Gold wire activation measurement

We use the activation method based on the gold wire (Au purity: >99.99%) in this study to measure the thermal neutron flux distribution along the beam direction [9]. The length of gold wire and its diameter is 200 mm and 0.5 mm, respectively. Since the epithermal neutron has a contribution to the gold activation, the cadmium (Cd) difference method is applied for determining the thermal neutron flux at different positions. Firstly, the gold wire put inside the water phantom is irradiated by the neutron beam. The irradiation time is two hours. Secondly, the gold wire covered with cadmium tube (inner diameter 1mm) (Cd purity: 99.95%) is irradiated. The wall thickness of the cadmium tube is 0.5 mm, which could effectively absorb the thermal neutron. The related irradiation time is five hours. The selection of irradiation time can guarantee that the counting rate of each gold wire pieces radioactivity is high enough, making the measurement time suitable. After neutron beam irradiation, each gold wire was cut into piece for 5mm and weighed. Subsequently, the radioactivity of each gold wire fragment is measured by a fully characterized High Purity Germanium (HPGe, GMX45 series by ORTEC) detector. Besides, the self-absorption correction coefficient of gold wire is 0.96. The initial calibration of the sensitivity of the HPGe was carried out by five point-like radionuclide photon sources instead of the gold wire, including ^{241}Am , ^{137}Cs , ^{60}Co , ^{133}Ba , and ^{152}Eu . For each of reference source, the confidence limits of the total error in determining the activity are less than 2%. In the procedure of the gamma measurement, the distance between the gold wire and the surface of the HPGe is about 15 cm, the error from the

shape difference of gold wire and point-like sources was estimated to be less than 1% by simulations.

The details of the estimation procedure for the thermal neutron flux from the data taken from HPGe are described in the following. First of all, the saturated reaction rates for each ^{197}Au atom without cadmium and with cadmium are calculated, which estimates the reaction rates between neutron and ^{197}Au under the situation of gold wire without cadmium and gold wire covered with cadmium. The formula for calculating this saturated reaction rate is shown in Eq. (1) [14].

$$(1)$$

where R denotes the saturated reaction rate, σ is the average cross-section of the ^{197}Au neutron capture reaction, Φ is the neutron flux at the gold wire piece we are considering, I denotes the number of protons per unit time during the irradiation, C is the net area of the full energy peak of the gold wire segment, which could be taken from the data of the HPGe, λ is the decay constant of ^{198}Au , ε is the detection efficiency of the HPGe, η is the branching ratio of ^{198}Au gamma rays, N is the total number of atoms in the gold wire segment, t_{irr} is the total irradiation time, t_c is the cooling time of the gold wire, and t_m is the detection time of the HPGe.

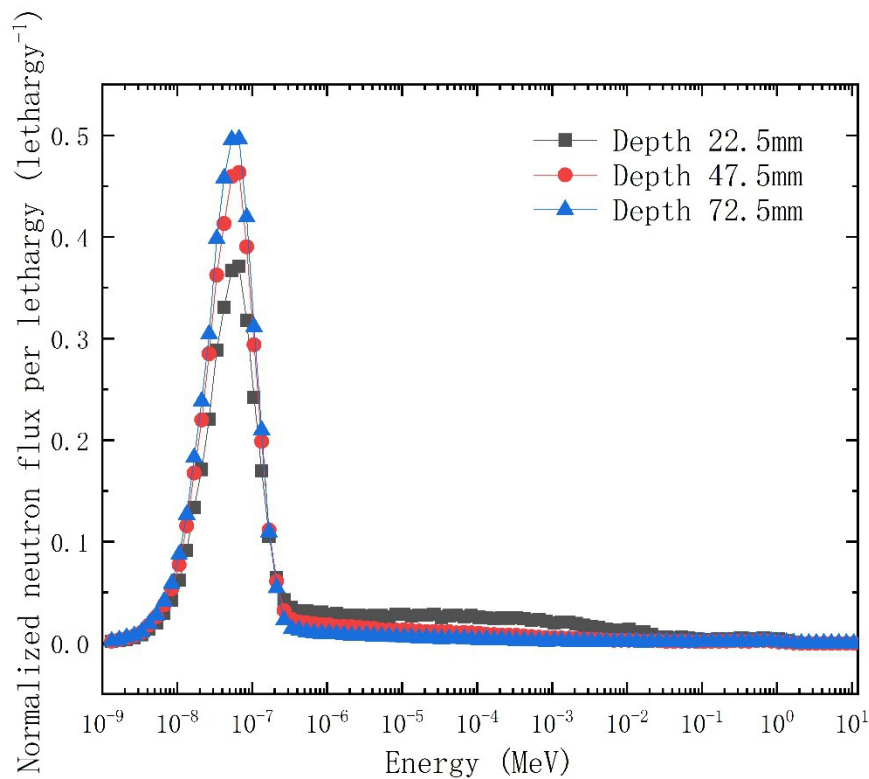


Fig.3 (Color online) Normalized neutron spectrum at different depth in the water

Figure 3 shows the normalized neutron spectrum at different depth in the water, and Fig.4 shows the saturated reaction rate versus depth in the water in the situation of bared gold wire and the gold wire covered with Cd. As the main function of the Cd is to absorb the thermal neutron because of its large thermal neutron capture cross-section ($2477 \times 10^{-24} \text{ cm}^2$ for natural Cd according to IRDFF[15,16]), the saturated reaction rate of the gold wire with Cd is related to the contribution of the epithermal neutrons. From Fig.3, the thermal neutron is dominant, and the thermal neutron ratio increases as the depth inside water increases. And from Fig.4, the saturated reaction rate of the bared gold wire is larger than that of gold wire covered with Cd. Particularly, the maximum saturated reaction rate of the bared gold wire is approximately five times higher than that with Cd. Thus, from the above analysis, the contribution for the gold wire activation mainly comes from thermal neutron. However, for attaining the more accurate result of thermal neutron flux depth distribution, the epithermal neutron contribution cannot be neglected, and the gold wire with Cd is still included in the measurement.

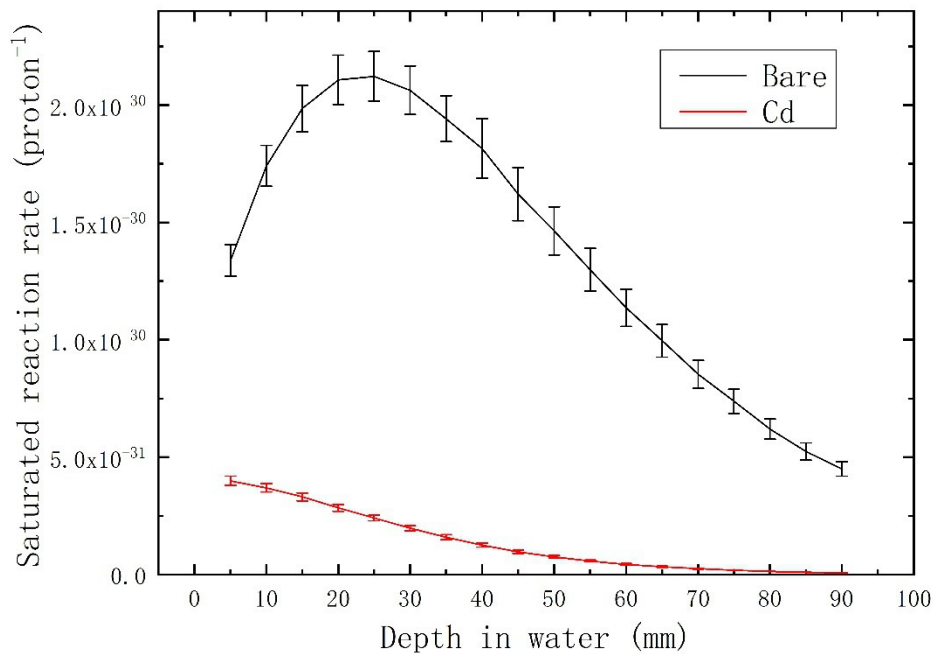


Fig.4 (Color online) Saturated reaction rate versus depth in the water.

Secondly, the thermal neutron flux at a specific position can be calculated in Eq.(2) [14]:

(2)

It is noted that Φ/I is the saturated reaction rate of the two situations described above. is the average thermal neutron absorbed cross-section of ^{197}Au . The above average cross-section is calculated by Eq.(3):

(3)

The neutron spectrum used in Eq. (3) is obtained by Monte Carlo simulation. The cross section data used in the Eq. (3) is taken from the Ref. [15] related to Au.

2.4 Indirect neutron radiography by Cu foil

In order to measure the 2D profile distribution of the neutron beam, we use indirect neutron radiography based on Cu sheet converter [10, 17]. The principles of this method may be summarized as follows.

A copper sheet was chosen as the activation material for its low-cost, good mechanical properties, a moderate thermal neutron capture cross section, and ideal half-life of the reaction products. There are two natural isotopes in copper, whose abundance are 69.2% and 30.8% for ^{63}Cu and ^{65}Cu , respectively. Because the half-life of the product of ^{66}Cu is around 5min, mainly released a gamma with energy of 1039 keV and branching ratio of 7%. It is regarded the chief contribution of gamma-activity of irradiated copper sheet is from the reaction of $^{63}\text{Cu}(n, \gamma)^{64}\text{Cu}$. Fig.5 shows the absorption cross section of ^{63}Cu (taken from ENDF/B-VII[15]), it shown its resonance peak to neutron is basically from several hundred eV to 100keV. The neutron flux in this energy region inside the water phantom can be negligible for the moderate effect by hydrogen in water. Thus, the total activation could be regard contributed by thermal neutrons. The size of the Cu sheet is 190 mm × 190 mm × 5 mm and the area of the Imaging Plate is 200 mm×200 mm. Since the thickness of the Cu is very small compared with the mean free path of the thermal neutron in Cu, the perturbation of the Cu sheet to the neutron field may be neglected.

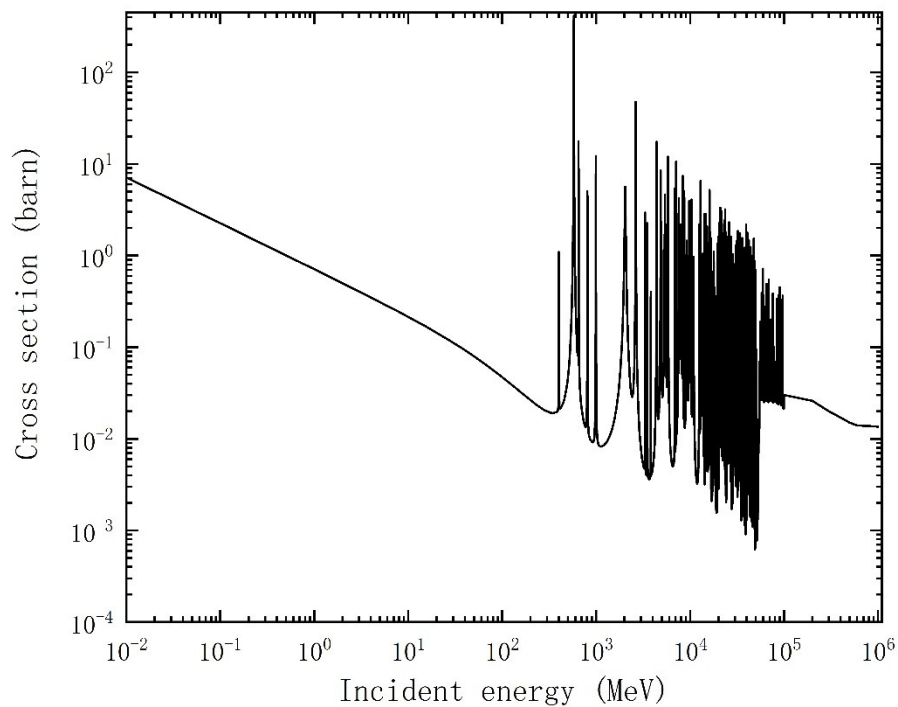


Fig.5 Neutron absorption cross section of ^{63}Cu [15]

The radioactivity at different positions on the Cu sheet is proportional to the thermal flux at that position. Thus, measuring the spatial radioactivity distribution of the Cu sheet provides information about the thermal neutron flux 2D distribution. We use a film-like Imaging Plate (BAS-MS manufactured by Fujifilm) to measure the gamma intensity distribution from the Cu sheets[10]. The principle of Imaging Plate detection is based on the "photostimulated luminescence" (PSL) phenomenon. The Imaging Plate is a flexible image sensor in which very small crystals of photo-stimulable phosphor of barium fluorobromide containing a trace amount of bivalent europium as a luminescence center, formulated as BaFBr:Eu^{2+} , are uniformly coated on a polyester support film. When the Imaging Plate is exposed to radiation, such as the gamma-ray, the above-designed phosphors can trap and store radiation energy. Based on the PSL phenomenon, this substance can emit light again upon the second stimulation by light having a longer wavelength than the wavelength of the first stimulation by the gamma radiation. Thus, the exposed Imaging Plate can be scanned with a laser beam of red light, releasing the stored information as light. Finally, the light is collected into the photomultiplier tube (PMT) and is converted to electric signals. Based on the above description, after irradiation, the Cu sheet is stick tightly to the Imaging Plate, which is read out by a Typhoon FLA 7000 (manufactured by GE), which provides the 2D intensity distribution.

2.5 Scintillator detector with scanning system

The measuring system involving scintillator detector consists of the following components [11]: a three-axis scanning platform, a natural lithium glass scintillator, an optical fiber, a silicon photomultiplier (SiPM), an electronics system, and data acquisition software, which are shown in Fig.6.

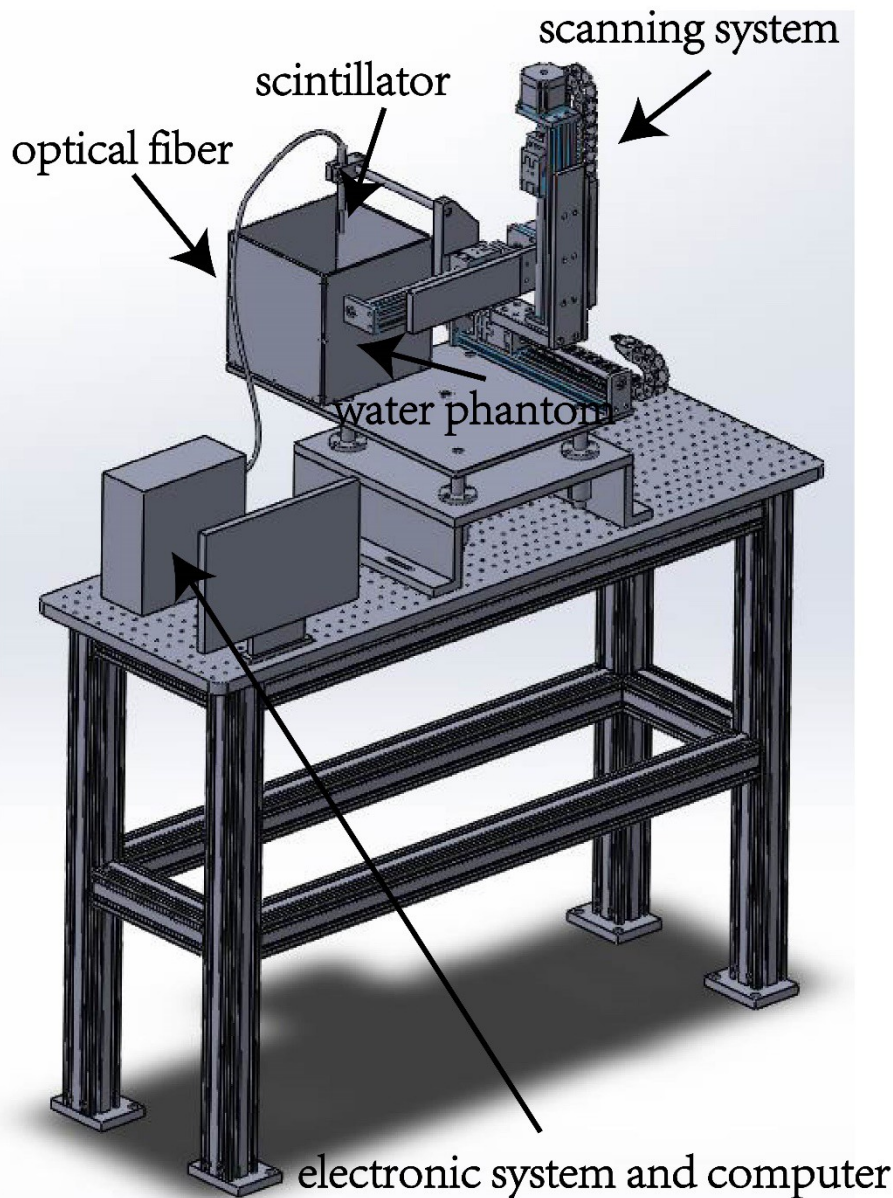


Fig.6 (Color online) Experimental setup.

The principle of the device can be described as follows. The BNCT facility generates the neutrons incident into the water phantom, and after gradually moderating, it occurs capture reaction with ${}^6\text{Li}$ in the lithium glass scintillator. The reaction releases charged particles to excite the materials in the scintillator, which causes it to emit scintillation light. And this light will be transferred into the amplified electrical signal by SiPM. The signal is handled by the electronics system and the data acquisition system.

As the neutron flux output from the facility is generally high, reaching the level of $1 \times 10^8 \text{ n/cm}^2/\text{s}$, the pulse pile-up effect due to the high thermal neutron intensity inside the water phantom should be avoided. The lithium glass scintillator was cut into the size of $1 \text{ mm} \times 1 \text{ mm} \times 1 \text{ mm}$ for this study. The small size of the detector could reduce the quantity of ${}^6\text{Li}$ atoms and reduces the thermal detection efficiency of the scintillator. Besides, the small size design can also bring about the better spatial resolution of the measuring device and further reduce the sensitivity to gamma rays. Moreover, scintillators with the natural abundance of ${}^6\text{Li}$ (7.5%) are selected, which can further reduce detection efficiency and ensure that the neutron detector is in normal pulse mode.

Since the scintillator is placed in the water phantom, in order to avoid the short circuit of the electric device and the performance reduction caused by the irradiation effect of the high-intensity neutron beam, an optical fiber with a length of about 2m was coupled at the back end of the scintillator. The scintillation light was transmitted to the outside of the water phantom for optical signal processing.

When the optical fiber is connected to a photoelectric conversion device, the scintillating light signal is converted to the electrical signal. Conventional photomultipliers usually have a large front window area and need to be supplied with a high-voltage power of about 1 kV. As the cross-sectional area of the optical fiber coupled with a small-size scintillator is relatively small, the conventional photomultiplier is not suitable in this case. In contrast, the silicon photomultiplier (SiPM) has the advantages of compact structure, small volume, large gain, low operating voltage, and fast time response [18, 19]. Thus, we select it as the photoelectric conversion device, which reduces the overall size of the measuring system, and improves the portability.

Besides, the SiPM output signals are sent to the electronic system for filtering, shaping, and amplification. And this electronic system includes the pre-amplifier, linear amplifier, amplitude discriminator, and ADC. The data acquisition software can receive, unpack, analyze, reconstruct, and save the neutron event data uploaded by the electronics. Moreover, the scintillator is attached to the scanning pole, which is driven by a stepping motor, to obtain the thermal neutron flux at any position in the water phantom. The motion of the scanning system could be controlled remotely by the computer. Finally, the whole system described above can achieve real-time measurement of the thermal neutron flux distribution inside the water phantom.

3. Result and analysis

3.1 Thermal neutron flux depth distribution

Figure 7 shows the thermal neutron flux depth distributions measured by gold wire and Cu foil compared to the Monte Carlo simulated distribution. Notice that the thermal neutron flux depth distribution of the Cu foil is extracted along the depth direction of the two-dimensional distribution data. It is noted that the Cu activation method is relative measurement instead of absolute measurement. The corresponding y-axis of the Cu result is in the right of Fig. 7. The errors of the gold wire measurements are about $\pm 10\%$. The simulated data have been multiplied by a normalization factor of 0.78 (ratio between peak value for the neutron flux obtained from measurement and peak value obtained from simulation), and after this correction, the thermal neutron flux depth distribution results by measurements and simulations are in good agreement. Results from simulation and Cu foil measurements are basically consistent. However, the peak value of Cu curve is at 20 mm, and the peak value of the simulation result is at 24 mm. At the same time, the tail of Cu foil method is slightly lower than that of the simulation. The Cu foil we use is a little bit out of shape and is not completely smooth when we put it in the water, resulting in the center line of the Cu foil is not consistent with the center line of the water phantom.

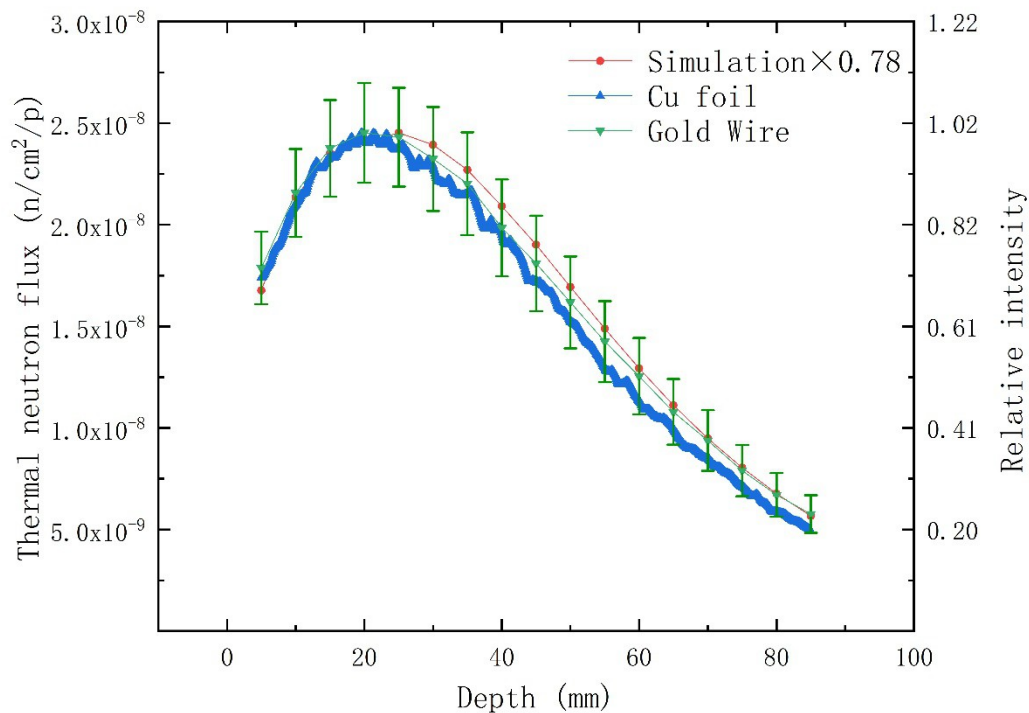


Fig.7 (Color online) Thermal neutron flux depth distribution as obtained by simulations, and measured by Cu foil and gold wire

Since the thermal neutron flux depth distribution in the water phantom is related to the neutron energy spectrum from the beam port, the good agreement between the simulated and measured curves shows that the beam energy spectrum of the facility is consistent with expected one. However, the actual spectrum at the beam port should be investigated in more details.

For obtaining the actual spectrum of the beam port, the neutron measurement without water phantom should be performed. Currently, it is difficult to carry out the measurement for the neutron spectrum of the full energy range with high accuracy [9]. The space of the D-BNCT01 irradiation room is limited, which means using the neutron time of flight method is difficult to achieve high energy resolution. Meanwhile, using multi-foil activation and Bonner sphere spectrometer can roughly estimate the neutron flux in different energy regions, but measuring the neutron spectrum with high energy resolution should be investigated further.

The above result of the water phantom shows that the distribution of measured result is consistent with the simulation result, which means the deviation between the actual neutron spectrum and simulated neutron spectrum at the entrance is so small. Thus, considering the final purpose of the BNCT is to irradiate the patient, the good agreement of the thermal neutron flux depth distribution in the water phantom between the measurement and simulation means the neutron spectrum generated by this facility is in line with the expectation and suitable for us to conduct the biological experiment.

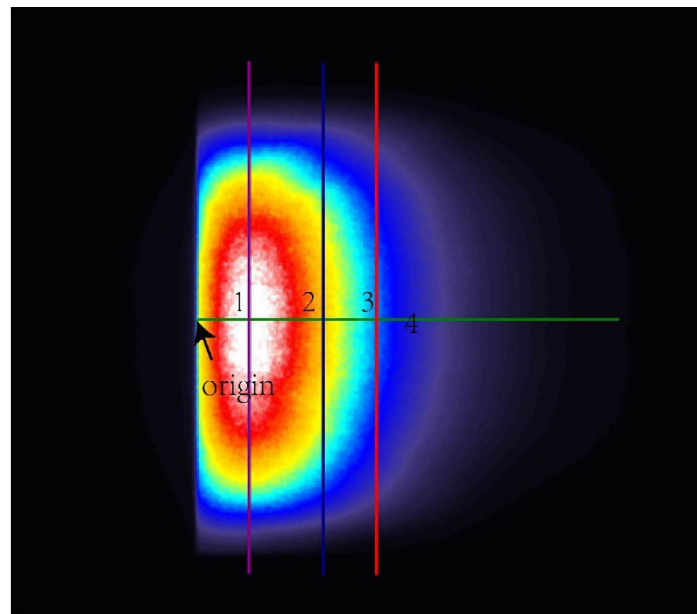
As mentioned above, the agreement between simulated and measured results is obtained by using a normalization factor 0.78 for the simulated data. The main deviation of absolute neutron flux between the measurement and simulation is due to the inaccuracy of the endfprot70 cross section of ENDF/VII library. And the deviation between the simulated BSA model and practical BSA structure also influences the above result. However, it is hard to describe the complete realistic structure of the facility in the model, especially for some tiny structure and some interstice between different components, which will also influence the neutron transportation in the facility. In current stage, it is difficult to obtain the precise simulation result by revising the double differential cross section of ${}^7\text{Li}(p, n){}^7\text{Be}$ and including the complete structure in the simulation model.

However, it is noted that this normalized factor is not fixed for the facility. Because the lithium target will be deteriorated and depleted [20, 21] when performing the long-term proton beam irradiation, which means the neutron yield of the lithium target will change as the running time gets longer. Meanwhile, when the lithium target is replaced, the neutron yield may also change. As the required irradiation time should be accurately evaluated when we perform the cell and animal experiments, the normalized factor should be corrected as the condition of lithium target changes. Thus, it is recommended that the phantom experiment should be conducted periodically to confirm the normalized factor, which is necessary before conducting the biological experiment.

Importantly, according to the simulation result of the neutron flux at the beam port and in the water phantom, we can deduce the neutron flux at the beam port from the maximum thermal neutron flux of the gold wire measurement and the normalized factor. The neutron flux at the beam port is 1.2×10^8 n/cm²/s under 5kW proton beam. As the BSA of the D-BNCT01 is designed for generating epithermal neutron, the direct epithermal neutron flux measurement at the beam port should be investigated in the future.

3.2 Result of Cu foil detection

Figure 8(a) shows the two-dimensional image intensity of the Cu sheet in the water phantom. As described above, the intensity distribution of this image can reflect the relative two-dimensional thermal neutron flux distribution in the water phantom. It is noted that the black area of the Fig.8(a) is the inactive area.



(a)

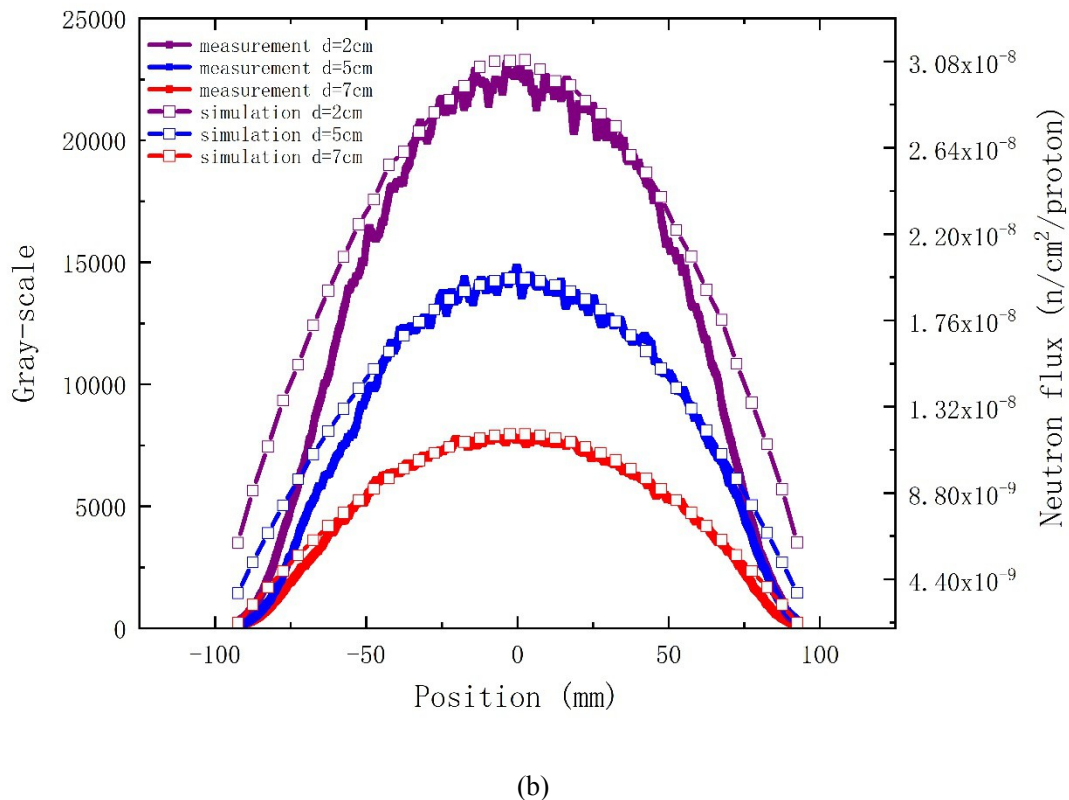


Fig.8 (Color online) Two-dimensional thermal neutron flux distribution. (a) image of the intensity for Cu foil. The depths of “1”, “2”, and “3” lines are 2 cm, 5 cm and 7 cm, respectively. The “4” line indicates the center axis of the water phantom. The origin is indicated by the arrow; (b) the lateral thermal neutron flux distribution from measurement and simulations at different depths (Depth (purple line)=2 cm, Depth (blue line)=5 cm, and Depth (red line)=7 cm).

The lateral thermal neutron flux distribution is basically symmetrical along the green line indicated in Fig.8(a). However, because of the inhomogeneity of the Cu density and the small deformation of the Cu foil, the perfect symmetry of the image is hard to obtain. Moreover, according to Fig.7 and Fig.8(a), the maximum thermal neutron flux is not in the front edge of the Cu foil. The position of the maximum thermal neutron flux is about 25mm depth in the water phantom. That is reasonable because the neutron beam generated by this facility is an epithermal neutron beam. Thus, the epithermal neutron is moderated by the front area of the water phantom, resulting in the maximum thermal neutron flux located at the deeper position. That is beneficial for treating the deeper tumor.

At the same time, Fig.8(b) shows the lateral thermal neutron distribution along with the three directions at the different depths indicated in Fig.8(a). The depth of the “1” line, “2” line, and “3” line in Fig.8(a) is 2cm, 5cm, and 7cm, respectively. And the simulation results are also shown in Fig.8(b), indicated as the curves with hollow squares. When considering the position between about -50mm to 50mm, the simulation results shown in Fig.8(b) are consistent with the measured results. However, the simulation results are higher than that of measurements in the margin area. This deviation is more obvious when closer to the edge. As the area of the Imaging Plate is close to that of the Cu foil, the above result shows that the response of the margin in the Imaging Plate we used is lower than that of its center. That means the gamma-ray detection efficiency of the Imaging Plate used in this experiment is different among different regions, especially in the margin area.

3.3 Result of scintillator detection

As for the result of the scanning scintillator, Fig.9 shows the results of the scintillator and the simulation. The three curves are normalized to peak value. However, we can see that the scintillator result is inconsistent with the result of the simulation. The scintillator curve is slimmer,

and the relative intensity at larger depth is smaller. The gray line denotes the thermal neutron flux distribution, and the red line the sums of fluxes coming from neutrons and gammas. The red curve is also slimmer than the gray one. It may be argued that the scintillator used in this research not only responds to neutrons but also to gamma rays. Although the gamma eliminating method is used by setting the threshold of the detection, the reaction rate of (n, γ) is significantly high because the thermal neutron flux is high in the water phantom. More gamma rays will be released, which will lead to the curve being "slimmer" after normalized to their peak value. Thus, for obtaining more accurate results of the scintillator, the procedure of reducing the gamma background further should be investigated in the future.

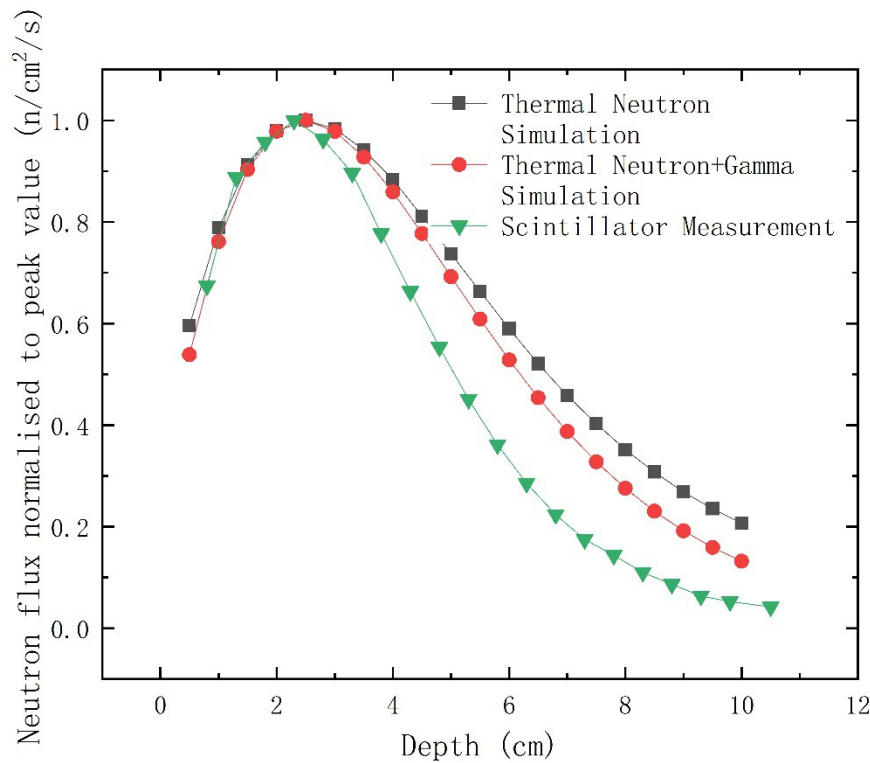


Fig.9 (Color online) Thermal neutron depth distribution including scintillator detection and simulation results of thermal neutron flux distribution and thermal neutron flux + gamma flux distribution.

4. Conclusion

An AB-BNCT instrument has been developed by the China Spallation Neutron Source team, which is referred to a D-BNCT01. The device is capable of generating high-intensity neutron beams. In this study, several experiments and measurements have been conducted to evaluate the neutron beam characteristics of D-BNCT01. In particular, we have performed measurements on a water phantom, using gold wire activation, Cu foil activation, and a scanning scintillator based on optical fibers, to measure the thermal neutron flux distribution. The relative thermal neutron distribution along the depth direction, as measured by gold wire and Cu foil activation is in good agreement with the simulation results. A factor 0.78 should be used to correct the simulation result for the absolute neutron flux. The neutron flux (using a 5 kW proton beam) at the beam port is estimated to be 1.2×10^8 n/cm²/s.

The two-dimensional thermal neutron flux distribution may be also measured using Cu foil activation, and results are consistent with those coming from Monte Carlo simulations between -50mm to 50mm. However, the thermal neutron distribution measured by scanning scintillator should be investigated further to eliminate the gamma-ray influence. Overall, in this paper, the current characteristics of the neutron beam at D-BNCT01 facility are evaluated, and the instrument is used to conduct cell and animal irradiation experiments.

Author contributions

All authors contributed to the study conception and design. Material preparation, data collection and analysis were performed by Jun-Yang Chen, Jian-Fei Tong, Zhi-Liang Hu, Xue-Fen Han, Bin Tang, Qian Yu, Rui-Qiang Zhang, Chong-Guang Zhao, Jun Xu, Shi-Nian Fu, Bin Zhou and Tian-Jiao Liang. The first draft of the manuscript was written by Junyang Chen and all authors commented on previous versions of the manuscript. All authors read and approved the final manuscript.

Funding

This work was supported by the Program for Guangdong Introducing Innovative and Entrepreneurial Teams (2017ZT07S225), the Institute of High Energy Physics Xie-Jialin Foundation (Grant No. Y95461F) and the National Natural Science Foundation of China (Grant No. U1932219).

Reference

- [1] M. Wang, Y. Tong, Q. Luo et al., Study of ATP borate ester effects on cell sensitization to radiation emitted by a nuclear reactor. Nucl. Sci. Tech. 31, 2 (2020). doi: [10.1007/s41365-019-0713-0](https://doi.org/10.1007/s41365-019-0713-0)
- [2] R.F. Barth, J.A. Coderre, M.G.H. Vicente et al., Boron neutron capture therapy of cancer: Current status and future prospects. Clin. Cancer Res. 11, 3987 (2005). doi: 10.1158/1078-0432.Ccr-05-0035
- [3] H. Hatanaka, Clinical results of boron neutron capture therapy. Basic Life Sci. 54, 15 (1990).
- [4] D.A. Allen, T.D. Beynon, S. Green, Design for an accelerator-based orthogonal epithermal neutron beam for boron neutron capture therapy. Med. Phys. 26, 71 (1999). doi: 10.1118/1.598479
- [5] D. Cartelli, M.E. Capoulat, T.J. Bergueiro et al., Present status of accelerator-based BNCT: Focus on developments in Argentina. Appl. Radiat. Isot. 106, 18 (2015). doi: 10.1016/j.apradiso.2015.07.031
- [6] C. Ceballos, J. Esposito, S. Agosteo et al., Towards the final BSA modeling for the accelerator-driven BNCT facility at INFN LNL. Appl. Radiat. Isot. 69, 1660 (2011). doi: 10.1016/j.apradiso.2011.01.032
- [7] T.A. Bykov, D.A. Kasatov, A.M. Koshkarev et al., A multichannel neutron flux monitoring system for a boron neutron capture therapy facility. J. Instrum. 14, P12002 (2019). doi: 10.1088/1748-0221/14/12/p12002
- [8] M. Kim, B.H. Hong, I. Cho et al., Design of a scintillator-based prompt gamma camera for boron-neutron capture therapy: Comparison of SrI2 and GAGG using Monte-Carlo simulation. Nucl. Eng. Technol. 53, 626 (2021). doi: 10.1016/j.net.2020.07.010
- [9] H. Kumada, K. Takada, S. Tanaka et al., Evaluation of the characteristics of the neutron beam of a linac-based neutron source for boron neutron capture therapy. Appl. Radiat. Isot. 165, 109246 (2020). doi: 10.1016/j.apradiso.2020.109246
- [10] P.E. Tsai, Y.H. Liu, H.M. Liu et al., Characterization of a BNCT beam using neutron activation and indirect neutron radiography. Radiat. Meas. 45, 1167 (2010). doi: 10.1016/j.radmeas.2010.07.008
- [11] A. Ishikawa, A. Yamazaki, K. Watanabe et al., A comparison between simulation and experimental results for depth profile of Li-6 reaction rate in a water phantom of BNCT using a small Li-6-based scintillator neutron detector with an optical fiber. Radiat. Meas. 133, 106270 (2020). doi: 10.1016/j.radmeas.2020.106270
- [12] L.S. Waters, G.W. McKinney, J.W. Durkee et al., The MCNPX Monte Carol radiation transport code, Paper presented at the Hadronic Shower Simulation Workshop (Batavia, IL, 6-8 Sep. 2007)
- [13] H. Liskien, A. Paulsen, Neutron production cross sections and energies for the reactions ^7Li (p, n) ^7Be and ^7Li (p, n) $^7\text{Be}^*$. At. Data Nucl. Data Tables. 15, 57 (1975). doi: 10.1016/0092-640X(75)90004-2
- [14] G.F. Knoll, Radiation detection and measurement, 4th edn. (John Wiley & Sons Inc., New Jersey, 2010), pp. 767-774
- [15] M.B. Chadwick, M. Herman, P. Oblozinsky et al., ENDF/B-VII.1 nuclear data for science and technology: cross sections, covariances, fission product yields and decay data. Nucl. Data

- Sheets 112, 2887 (2011). doi: 10.1016/j.nds.2011.11.002
- [16] A. Trkov, P.J. Griffin, S.P. Simakov et al., IRDFF-II: A new neutron metrology library. Nucl. Data Sheets 163, 1 (2020). doi: 10.1016/j.nds.2019.12.001
- [17] Y.H. Liu, C.K. Huang, P.E. Tsai et al., BNCT epithermal neutron beam mapping by using indirect neutron radiography. Nucl. Technol. 168, 354 (2009). doi: 10.13182/nt09-a9208
- [18] F. Acerbi, S. Gundacker, Understanding and simulating SiPMs. Nucl. Instrum. Methods Phys. Res. A 926, 16 (2019). doi: 10.1016/j.nima.2018.11.118
- [19] P.P. Calo, F. Ciciriello, S. Pettrignani et al., SiPM readout electronics. Nucl. Instrum. Methods Phys. Res. A 926, 57 (2019). doi: 10.1016/j.nima.2018.09.030
- [20] S. Nakamura, H. Igaki, M. Ito et al., Neutron flux evaluation model provided in the accelerator-based boron neutron capture therapy system employing a solid-state lithium target. Sci. Rep. 11, 8090 (2021). doi: 10.1038/s41598-021-87627-8
- [21] S. Nakamura, H. Igaki, M. Ito et al., Characterization of the relationship between neutron production and thermal load on a target material in an accelerator-based boron neutron capture therapy system employing a solid-state Li target. PLoS One 14, e0225587 (2019). doi: 10.1371/journal.pone.0225587